

Dielectric Properties of Pure and Gd-Doped HfO₂ Ceramics

Chunchang Wang,[†] Da Zhang, Hong Wang, Yi Yu, Yide Li, and Qiuju Li

Laboratory of Dielectric Functional Materials, School of Physics & Material Science, Anhui University, Hefei 230601, China

The pure, 2 at.%, and 20 at.% Gd-doped HfO₂ ceramics were prepared by the standard solid-state reaction technique. Dielectric properties of these ceramics were investigated in the temperature range 300–1050 K and frequency range 20–5 × 10⁶ Hz. Our results revealed an intrinsic dielectric constant around 20 in the temperature below 450 K for all tested ceramics. Two oxygen-vacancy-related relaxations R1 and R2 were observed at temperatures higher than 450 K, which were identified to be a dipolar relaxation due to grain response and a Maxwell–Wagner relaxation due to grain-boundary response, respectively. The dielectric properties of the pure and slightly doped (2 at.%) samples are dominated by the grain-boundary response, which results in a colossal dielectric behavior similar to that found in CaCu₃Ti₄O₁₂. The doping level of 20 at.% leads to the structural transformation from monoclinic phase to cubic phase. The dielectric properties of the heavily doped HfO₂ are dominated by the grain response without any colossal dielectric behavior.

I. Introduction

Hafnium oxide (HfO₂) is known as a promising high-κ insulator playing an increasing important role in micro-electric devices.¹ From the view point of application, the knowledge of the dielectric properties of HfO₂ in both thin film and ceramic cases is of vital importance. Most of the existing reports on the dielectric properties of HfO₂ were performed theoretically.^{2–5} It was revealed that oxygen vacancies are the decisive fact in controlling the electric and dielectric properties of HfO₂.^{6–8} In contrast to the abundant theoretical results, experimental investigations were solely focused on the thin film case.^{9–15} Ferroelectricity had been widely reported recently in HfO₂ thin films via slightly doping with different cations such as Gd, Al, Y, and Si.^{16–20} This result is quite astonishing because ferroelectricity is physically prohibited in bulk HfO₂ as it exhibits a centrosymmetrically monoclinic structure at room temperature. The capping material was reported to be crucial for ferroelectricity in HfO₂ thin films.²⁰ Very recently, Sang et al.²¹ confirmed that a non-centrosymmetric *Pca*2₁ orthorhombic phase exists in Gd:HfO₂ thin films, which provides a structural origin for ferroelectricity in the doped films.

The above results indicate that the dielectric properties of HfO₂ are far from well characterized and motivate our research interesting on the dielectric properties of the bulk counterpart. We, herein, present a study on the dielectric properties of both pure and Gd-doped HfO₂ ceramics in the temperature range 300–1050 K and frequency range 20–5 × 10⁶ Hz. Our results showed that the dielectric properties of these samples are strongly related to the oxygen vacancies.

II. Experimental Details

The pure, 2 at.%, and 20 at.% Gd-doped HfO₂ ceramics, referred to as samples 1, 2, and 3, respectively, were prepared by the standard solid-state reaction technique. High-purity (99.99%) starting powders of HfO₂ and Gd₂O₃ powders were thoroughly mixed using a mortar and calcined at 1200°C for 10 h and 1400°C for 10 h with intermediate grinding. The resultant powders were reground and pressed into pellets with size of 12.3 mm in diameter and about 0.76 mm in thickness and finally sintered at 1400°C for 24 h followed by furnace cooling to room temperature. The crystal structure was characterized by X-ray diffraction (XRD) performed on a MXP18AHF diffractometer (MARK, Mac Science Co. Ltd., Yokohama, Japan) with Cu Kα radiation. The morphology and microstructure of the sintered samples were characterized by a field-emission scanning electron microscopy (SEM) (Model S-4800; Hitachi Co., Tokyo, Japan). The temperature-dependent dielectric and electric properties were obtained using a Wayne Kerr 6500B precise impedance analyzer (Wayne Kerr Electronic Instrument Co., Shenzhen, China) with the sample mounted in a holder placed inside a PST-2000HL dielectric measuring system (Partulab Co., Wuhan, China). The temperature variations were automatically controlled by a Stanford temperature controller with a heating rate of 2 K/min. The amplitude of the ac measuring signal was 100 mV rms. Annealing treatments were performed in flowing (200 mL/min) O₂ and N₂ (both with purity >99.999%). Before measuring, electrodes were made by printing silver paste on both sides of the disk-shaped samples and then fired at 600°C for 1 h to remove the polymeric component.

III. Results and Discussion

The XRD patterns of the three samples were shown in Fig. 1 recorded at room temperature. It is seen that the low doping concentration of 2 at.% Gd₂O₃ has no evident influence on the crystal structure. Both samples 1 and 2 exhibit monoclinic phase. The patterns can be indexed according to JCPDS No. 74-1506. The lattice parameter calculated by MDI Jade 5.0 software (Materials Data Inc., Livermore, CA) are listed in Table I. When Gd₂O₃ concentration reaches 20 at.%, the crystal structure transfers to the cubic phase with the lattice parameter $a = 5.263$ Å. This finding agrees well with that reported in literature.²²

The insets (a), (b), and (c) are the surface images of samples 1, 2, and 3, respectively. As observed, samples 1 and 2 show condensed morphology composed of larger grains coexisting with smaller ones. The grains are separated by distinct grain boundaries. Their density is ~90% of the theoretical density, as determined by an Archimedes method. Slight doping of Gd₂O₃ leads to the reduction in the fraction of smaller grains. The average grain size was estimated to be 9.6 and 12.6 μm for samples 1 and 2, respectively. However, when the doping level was elevated to 20 at.%, great changes were observed: the grains become much smaller but more uniform and the morphology contains a large number of pores. The density reduces to 85% of the theoretical value. The average grain size is about 3.47 μm. These changes can be ascribed to the structural phase

J. Ihlefeld—contributing editor

Manuscript No. 36791. Received April 26, 2015; approved July 26, 2015.

[†]Author to whom correspondence should be addressed. e-mail: ccwang@ahu.edu.cn

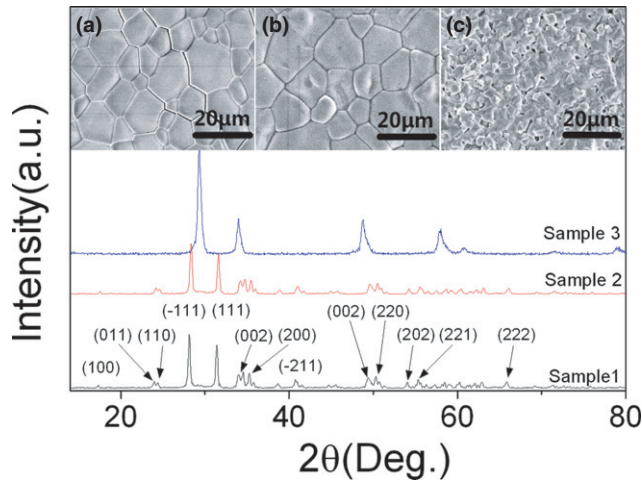


Fig. 1. X-ray diffraction patterns for the pure and Gd-doped HfO_2 ceramics. Insets (a), (b), and (c) are the SEM micrographs of samples 1, 2, and 3, respectively.

Table I. Lattice Parameters for Samples 1, 2, and 3

Sample no.	Lattice parameter (Å)		
	<i>a</i>	<i>b</i>	<i>c</i>
1	5.172	5.201	5.389
2	5.119	5.171	5.306
3	5.263		

transition. Because no Gd_2O_3 phases were observed in sample 3 indicating that Gd_2O_3 could be accommodated in solid solution in the HfO_2 matrix. The replacement of Hf^{4+} ions (0.086 nm) by Gd^{3+} ions (0.093 nm) leads to obvious lattice distortion, thereby limiting the cubic grain growth.²³

Figures 2(a) and (b) present, respectively, the temperature (T) dependence of the dielectric constant ϵ' (the real part of the complex permittivity ϵ^*) and dielectric loss tangent ($\tan \delta = \epsilon''/\epsilon'$, where ϵ'' is the imaginary part of the complex permittivity) of pure HfO_2 measured under various frequencies. It is seen that the sample shows colossal dielectric constant (CDC) behavior similar to that found in $\text{CaCu}_3\text{Ti}_4\text{O}_{12}$ (CCTO).²⁴ The CDC behavior of HfO_2 takes place in the temperature higher than 450 K. It is composed of two frequency dispersion sigmoidal steps occurring around 500 and 800 K in the dielectric constant. The steps are accompanied by two sets of peaks in the corresponding curve of dielectric loss tangent. The peak position shifts to high temperature as the measuring frequency (f) increases, indicating that there are two thermally activated relaxation processes in the sample. For brevity, these relaxations are named as R1 and R2 in the order of ascending temperature (descending frequency). In the temperature range below 450 K, both $\epsilon'(T)$ and $\tan \delta(T)$ become flat curve independent of frequency and temperature. This signals the intrinsic dielectric response resulting from the electronic and/or ionic polarization. This point was further confirmed by impedance analysis. The inset of Fig. 2 shows the spectroscopic plots of the impedance, $Z''(f)$, at selected temperatures. One notes that the curves recorded below 450 K overlap leading to a master linear straight line with a slope of -1 in the double logarithmic coordinate frame. This finding reveals that the tested cell is an ideal capacitor with the HfO_2 being the ideal insulator, because the capacitance of an ideal capacitor is described by

$$Z^* = 1/(j\omega C) \text{ or } Z'' = -1/(\omega C) \quad (1)$$

where C is the capacitance of the measured cell, j is the imaginary unit, and $\omega = 2\pi f$ is the angular frequency. When

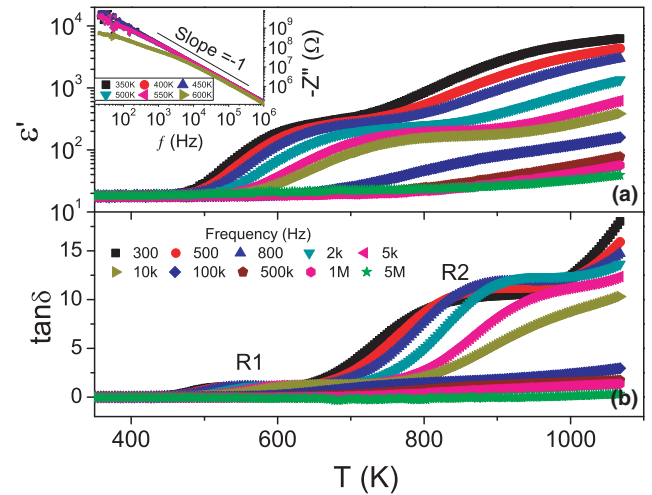


Fig. 2. Temperature dependence of the dielectric constant ϵ' (a) and dielectric loss tangent $\tan \delta$ (b) for the pure HfO_2 sample measured under different frequencies. Inset shows the frequency dependence of the imaginary part of impedance Z'' for sample recorded at several temperatures.

the measuring temperature is higher than 500 K, the low-frequency data points in the spectroscopic plot deviate from the linear line, indicating that leaky current due to relaxation occurs in the tested cell. The cell can no longer be considered as an ideal capacitor. This finding confirms the intrinsic dielectric response below 450 K. The intrinsic dielectric constant is found to be 18.06 and the loss tangent value in the intrinsic range is 0.025. Such features of low dielectric loss, high (with respect to the dielectric constant of 8.9 for Si_3N_4) and both temperature and frequency independent dielectric constant over a wide temperature up to 450 K, make HfO_2 very desirable for gat dielectric material.

Sample 2 shows similar dielectric behavior to that of sample 1 (not shown). No trace of ferroelectricity was found. It is worth pointing out that the stress/strain induced due to the different lattices and/or crystallographic symmetries between the film and substrate plays a very active role on the properties of the thin film system. It had been reported that the electric field induced by strain can enhance the ferroelectric polarization,²⁵ and can even transform a paraelectric material such as SrTiO_3 to a ferroelectric phase.²⁶ The absence of ferroelectricity in sample 2 may be attributed to the strain. We, therefore, turn our attention to the dielectric properties of the heavily doped sample. Figure 3 shows the temperature dependence of dielectric constant of sample 3. When compared with sample 1, two features can be extracted: (1) The heavily doped sample shows a higher dielectric constant plateau of 22 in the same temperature range below 450 K. (2) The first stepwise increase becomes much weaker and instead of the second stepwise increase, a nearly exponential increase in $\epsilon'(T)$ appears when temperature is higher than 800 K. This leads to the disappearance of the CDC behavior. The rapid increase in $\epsilon'(T)$ strongly signals that the conductivity dominates the dielectric response and implies that Gd doping can improve the conductivity. The inset is the temperature dependence of the dielectric loss tangent of sample 3. The two relaxations behave as humps further confirming the pronounced conductivity that creates remarkable background.

Relaxation parameters are important for understanding the mechanisms of R1 and R2. To obtain the relaxation parameters, accurate peak positions (T_p) of the relaxations are needed. In doing so, nonlinear fittings with two Debye peaks were applied to fit the $\tan \delta(T)$ curves. As an illustration, the resultant fitting curve and relaxations R1 and R2 (solid lines) as well as the background (dashed line) to the experimental data points (open circles) recorded at 300 Hz

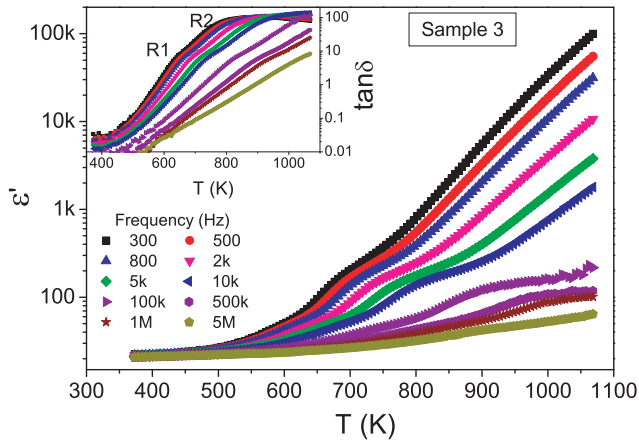


Fig. 3. Temperature dependence of the dielectric constant for sample 3. Inset shows the temperature dependence of $\tan \delta$ for the sample.

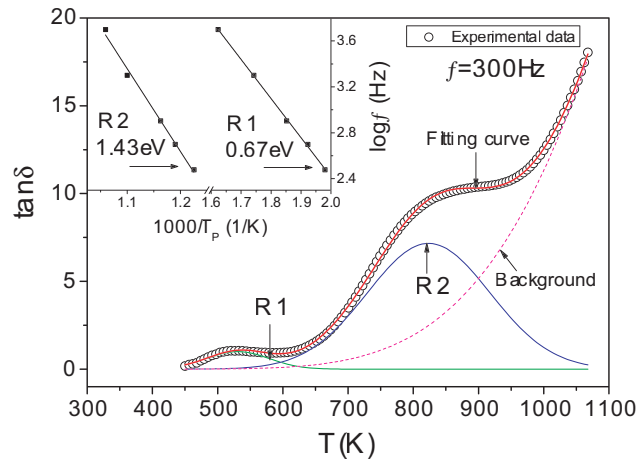


Fig. 4. A representative example showing the comparison between the experimental data (open circles) of $\tan \delta(T)$ recorded at 300 Hz for the pure sample and the fitting curve and resulting peaks (solid lines) as well as the background (dashed line). Inset shows the Arrhenius plots for R1 and R2 with the data deduced from the fitting results.

for sample 1 were displayed in Fig. 4. The fitting curve matches the experimental data very well, indicating perfect fitting result was achieved. The net peak intensity of R2 is much higher than that of R1, indicating that R2 is the predominant contributor to the CCTO-like dielectric behavior of pure HfO_2 . The relaxation parameters for R1 and R2 can be deduced in terms of the Arrhenius law:

$$f = f_0 \exp(-E_a/k_B T_p) \quad (2)$$

where f_0 is the pre-exponential factor, E_a is the activation energy of relaxation, and k_B is the Boltzmann constant. The inset of Fig. 4 shows the Arrhenius plots of R1 and R2 for sample 1. The calculated values of E_a and f_0 for the three tested samples are tabulated in Table II. The activation energy for R1 and R2 was found to be around 0.7 and 1.2 eV, respectively. It was widely reported that relaxations in oxides with the activation energy around 0.7 and 1.2 eV are oxygen-vacancy-related relaxations.^{27–29} Our recent work pointed out that the relaxation caused by the electromigration of oxygen vacancies at high temperatures is a kind of conduction relaxation rather than the conventional dielectric relaxation in high-resistive materials.^{30,31} The electrical response due to the electromigration of oxygen vacancies can

Table II. Relaxation Parameters for Samples 1, 2, and 3 Obtained from the Dielectric Permittivity/Electric Modulus Spectra

Sample no.	R1		R2	
	E_a (eV)	f_0 ($\times 10^9$ Hz)	E_a (eV)	f_0 ($\times 10^{11}$ Hz)
1	0.67/0.77	1.69/5.81	1.43	1.95
2	0.70/0.79	1.17/1.29	1.07	0.53
3			1.36/1.28	3400/1199

be described by the well-known power law, that is, the universal dielectric response (UDR).³²

$$\varepsilon'' = B(T)\omega^{s-1} \quad (3)$$

$$\varepsilon'' = \varepsilon_\infty + C(T)\omega^{s-1} \quad (4)$$

where ε_∞ is the dielectric constant at high-frequency limit, $B(T)$, $C(T)$, and s (with the value between 0 and 1) are temperature-dependent constants.

Contrary to the dielectric relaxation, which shows a semi-circle in the Cole–Cole plot (i.e., ε'' is plotted against ε'), the conduction relaxation as described by Eqs. (3) and (4) behaves as a straight line at a given temperature. Figures 5 (a) and (b) shows such plots for samples 1 and 3, respectively. For sample 1, perfect straight lines can be seen at temperatures lower than 800 K. However, the corresponding slope changes when increasing the temperature up to 825 K. The data points at the lowest frequencies obviously deviate from the linear relation leading to two linear segments. This finding implies that conductive mechanism changes in the temperature range 800–825 K. A new conductive mechanism comes into action at higher temperatures. The temperature range that the conductive mechanism changes matches well with the temperature range where R2 occurs as seen in Fig. 1(a). This finding indicates that the observed relaxations are closely related to the conductive processes. The hopping motions of oxygen vacancies can create reorientational dipole relaxation.²⁷ Our recent report revealed that when the hopping vacancies were blocked by grain boundaries forming space-charge therein, a Maxwell–Wagner relaxation occurs at higher temperatures.³³ The R1 and R2 might be related to the bulk (grain) and grain-boundary responses, respectively. It was widely reported that the relaxation intensity of an oxygen-vacancy-related relaxation depends on the concentration of the vacancies and can be tuned by annealing in N_2 and/or O_2 atmospheres.³⁴ If the annealing treatments were performed at a sufficiently lower temperature than that of sintering for not too long time, the properties of the grains would have no significant variation, whereas the nature of the grain boundaries can be obviously changed. As a result, the dielectric relaxation related to the (grains) grain boundaries is expected to be (insensitive) sensitive to these annealing treatments.³⁵ To confirm this inference, annealing treatments first in O_2 and then in N_2 were performed at 800°C far away from the sintering temperature (1400°C) for 2 h. After each treatment, dielectric properties were measured as a function of temperature. Figure 6 compares the temperature dependence of the loss tangent record at 300 Hz in the as-prepared, O_2 - and N_2 -annealed cases. To get a clear picture about how the peak intensity varies with the annealing treatments, nonlinear fittings were applied. The left and right insets are the resulting peak of R1 and R2, respectively. As expected, R1 is almost independent of these treatments, whereas R2 is depressed by O_2 -annealing and then enhanced by the N_2 -annealing. These findings further support that R1 and R2 resulting from the bulk and grain-boundary responses, respectively.

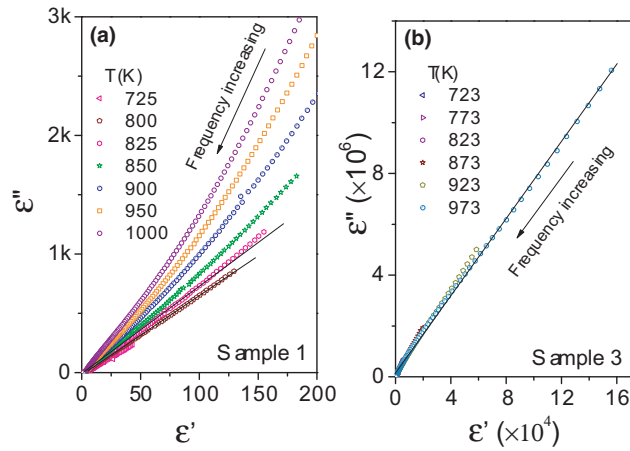


Fig. 5. The Cole–Cole plots for samples 1 (a) and 3 (b) recorded under different temperatures. The straight lines are guides to the eyes.

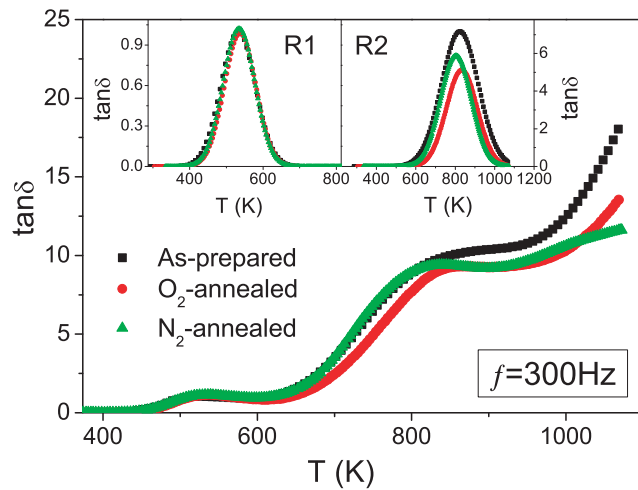


Fig. 6. Temperature dependence of $\tan \delta$ at 300 Hz for a pure HfO_2 sample before (as prepared) and after being annealed in O_2 and N_2 . The left and right insets are the fitting peaks for R1 and R2, respectively.

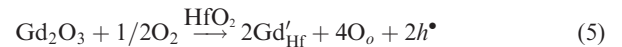
For sample 3, the Cole–Cole plot [Fig. 5(b)] shows almost one linear segment without any obvious deviation of the data points. It seems that the sample possesses one relaxation process. This is contrary to the finding of Fig. 3. A careful examination reveals a weak deviation from the linear segment for the data points in the high-frequency range. This indicates that the linear segment is contributed by the data points in the low-frequency range. Hence, the dielectric properties of sample 3 are dominated by R2, because the relaxation in the low (high)-frequency (temperature) range corresponds to R2. This point is further confirmed by the results from the electric modulus spectra.

The electric modulus is defined as $M^* = M' + jM'' = 1/\epsilon^*$, which shares the same mechanism as that of the dielectric permittivity. Figures 7(a), (b), and (c) show, respectively, the spectroscopic plots of the electric modulus for samples 1, 2, and 3 recorded at a series of temperatures. From which we can see that, aside from a pronounced high-frequency peak, a low-frequency hump can be seen in samples 1 and 2. The low- and high-frequency peaks can be identified to be R2 and R1, respectively, whereas for sample 3, only the pronounced peak can be seen. Arrhenius plot of the pronounced peak was displayed in Fig. 7(d) and the deduced values of E_a and f_0 are shown in Table II. One notes that the relaxation parameters of the pronounced peak for samples 1 and 2 pertain to those of R1 deduced from the spectra of $\tan \delta(T)$,

confirming that the pronounced high-frequency peak in the two samples corresponds to R1. However, the relaxation parameters of the pronounced peak for samples 3 are comparable with those of R2 deduced from the $\tan \delta(T)$ spectra. This finding evidences that R2 of samples 3 prevails over R1 becoming the dominant relaxation response in the electric modulus spectra. Meanwhile, the finding implies that R1 of samples 3 moves to a higher frequency range referenced to samples 1 and 2, and becomes much weaker and/or very close to R2 as it is not detectable even in the bilogarithmic representation.

To decipher why R1 is not detectable in Fig. 7(c), Fig. 8 presents the comparison of the normalized spectroscopic plot of the electric modulus for the three samples. In Fig. 8 each M'' and f were normalized with respect to the peak position M''_{\max} and f_p , respectively. The normalized spectroscopic plot for sample 1 recorded at 650 K is asymmetric because of the relaxation R1 as indicated by the low-frequency hump. Free from the interference of R1 [see Fig. 7(b)], the normalized spectroscopic plot for sample 2 recorded at 473 K is symmetric with a width of the peak at half-maximum found to be 1.498. This value is larger than 1.144 for the ideal Debye relaxation.³⁶ The deviation from the ideal Debye relaxation can be well explained by the fact that the strong interaction between oxygen vacancies and their surrounding medium leads to the spread of relaxation time.³⁰ The low-frequency wing of the normalized spectroscopic plot for sample 3 recorded at 673 K falls onto the curve of sample 2. But the high-frequency wing goes outward leading to an asymmetric peak. This fact convincingly evidences the existence of a weak peak close to the normalized peak in the high-frequency range. As the normalized peak of sample 3 is R2, the shadowed high-frequency peak can be identified to be R1.

A pertinent question is why R2 becomes the dominant relaxation in sample 3, whereas R1 is the dominant relaxation in samples 1 and 2 in the electric modulus spectra. To answer this question, impedance analysis was performed. Figures 9(a) and (b) present the Nyquist plot (Z'' versus Z' , where Z' and Z'' are the real and imaginary parts of the complex impedance Z^*) for samples 1 and 3, respectively. An asymmetric semicircle can be seen for both samples. The apex of the semicircle of sample 3 is much smaller than that of sample 1 further confirming that Gd doping can improve the conductivity. This fact can be explained in terms of the following defect equation:



It is seen that the gadolinium acts as acceptor that introduces electron holes, thereby improving the conductivity.

The asymmetric semicircle indicates that it is composed of overlapped arcs due to different contributions. To identify these contributions, Figs. 9(c) and (d) replot the isotherm in Figs. 9(a) and (b), respectively, using an alternative representation of Z' versus $-Z''/f$. In this kind of representation, three sectional straight lines can usually be obtained with the sequential regions from low to high frequencies corresponding, respectively, to the dielectric response from the contacts, grain boundaries, and bulk grains.³⁷ Each section can be modeled by a parallel-connected RC (R = resistor, C = capacitor) unit. The product of RC represents the relaxation time $\tau_i = R_i C_i$ ($i = g, gb, \text{ and } c$ denoting the grain, grain boundary, and sample-electrode contact, respectively), which yields a peak in the Nyquist plot when $\omega\tau_i = 1$ is fulfilled. In addition, the slope of the linear section in Figs. 9(c) and (d) is given by $f_i = 1/\tau_i = 1/(R_i C_i)$.³⁸ Sample 1 shows three well-clarified sections of the grain, grain boundary, and sample-electrode contact, according to different slopes of the three sections. The demarking frequencies separating these sections were found to be 1998 and 1.10×10^5 Hz. The high- and

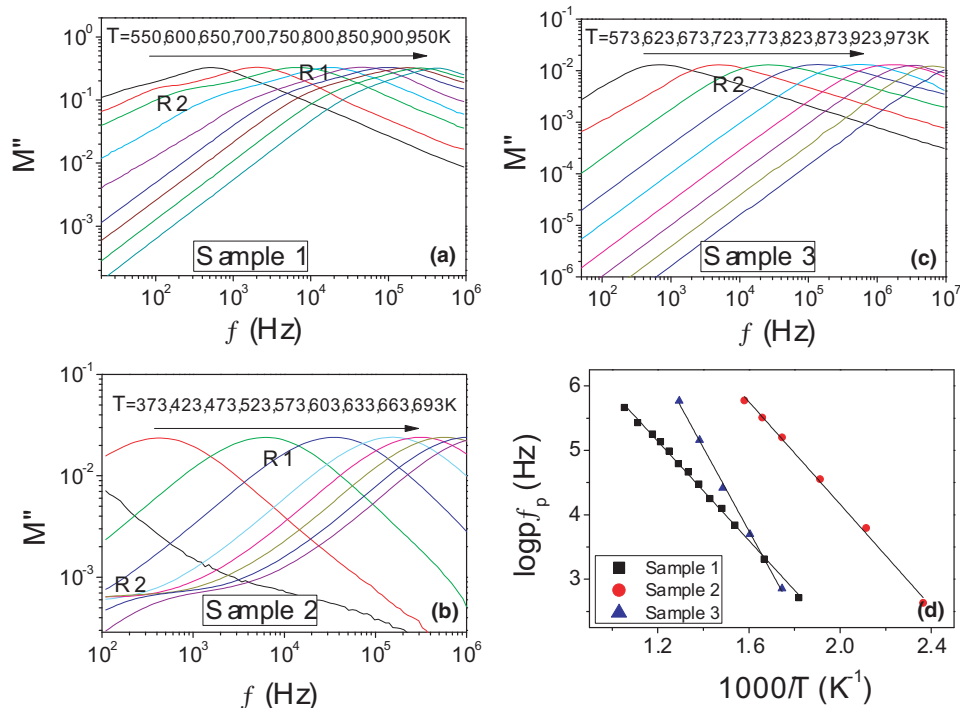


Fig. 7. (a), (b), and (c) The electric modulus spectroscopic plots for samples 1, 2, and 3, respectively. (d) The Arrhenius plots of the pronounced peak found in the electric modulus plots for the samples.

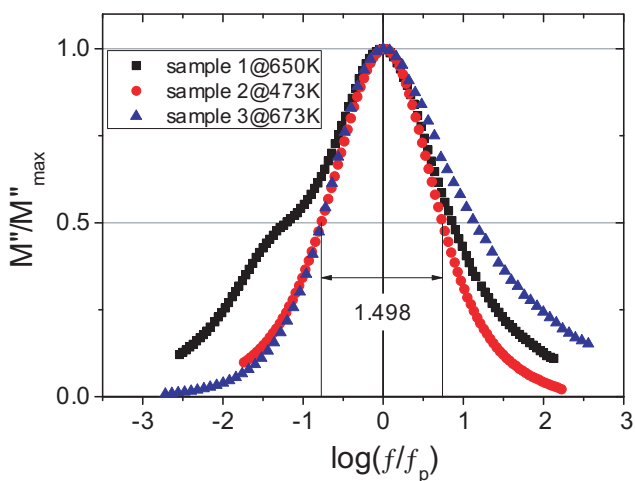


Fig. 8. The normalized electric modulus M''/M''_{\max} versus the reduced frequency f/f_p .

low-frequency relaxations (R1 and R2) in the modulus spectra [Fig. 7(a)], taking the isotherm recorded at 800 K as an example, occur around 1.14×10^5 and 5952 Hz, which can be identified to be related to the grain and grain-boundary contributions, respectively. This result further convinces that, similar to CCTO, the CDC behavior found in pure HfO_2 and slightly doped sample has an extrinsic Maxwell–Wagner nature due to grain-boundary relaxation. The absence of the contact contribution in the modulus spectra can be well understood based on the fact that the modulus spectra emphasize the contribution with low capacitance, whereas the impedance spectra highlight the contribution with large resistance.³⁹ Likewise, the demarking frequencies for sample 3 were found to be 2.23×10^5 and 2.93×10^6 Hz. The R2 peak in the modulus spectra [Fig. 7(c)] recorded at 823 K occurs around 1.79×10^6 Hz, which belongs the grain-boundary response.

The grain and grain-boundary sections of sample 3 have approximate the same slope. This is the reason that R1 and R2 are almost overlapped in the modulus spectra as

confirmed in Fig. 8. The similar slopes of the grain and grain-boundary sections indicate $f_g = 1/(R_g C_g) \sim f_{gb} = 1/(R_{gb} C_{gb})$. As $R_g < R_{gb}$ [c.f. Fig. 9(d)], one has $C_g < C_{gb}$. Therefore, the modulus spectra emphasize the small-capacitance relaxation. This is the reason that R2 rather than R1, as found in samples 1 and 2, becomes the dominant relaxation in sample 3. The small capacitance is also evidenced by the SEM images shown in Fig. 1, which reveals that samples 1 and 2 have larger grains than that of sample 3. According to Adams et al.,⁴⁰ ceramics with a small grain size have larger fraction of volume taken by Schottky barriers resulting in an increase in the effective thickness of the charge storage regions. Although the charges are stored at the grain boundaries, the thickness of the grain-boundary capacitance of sample 3 is larger. This produces a smaller value of C_{gb} for sample 3.

In summary, the grain response dominates the electric modulus spectra of samples 1 and 2, whereas the grain-boundary response dominates the spectra of sample 3. Based on the brick-layer model, the dielectric properties of the tested sample can be modeled by two RC units connected in series [inset of Fig. 9(a)] with one for the grain and the other for the grain boundary.⁴¹ As a consequence, the measured dielectric properties are controlled by the contributor with relatively larger capacitance, the dielectric properties of samples 1 and 2 are, therefore, dominated by the grain-boundary response, whereas the dielectric properties of sample 3 is dominated by the grain response.

IV. Conclusion

We present a comparative study on the dielectric properties of pure and Gd-doped (with the doping level of 2 at.% and 20 at.%) HfO_2 ceramics. The pure and slightly doped (2 at.%) samples show CDC behavior composed of two oxygen-vacancy-related relaxations (R1 and R2) in the temperature range higher than 450 K. The low-temperature relaxation (R1) was argued to be a dipolar relaxation due to the hopping motions of oxygen vacancies inside grains, whereas the high-temperature one was ascribed to be a Maxwell–Wagner relaxation caused by grain-boundary response. The CDC behavior is dominated by the Maxwell–

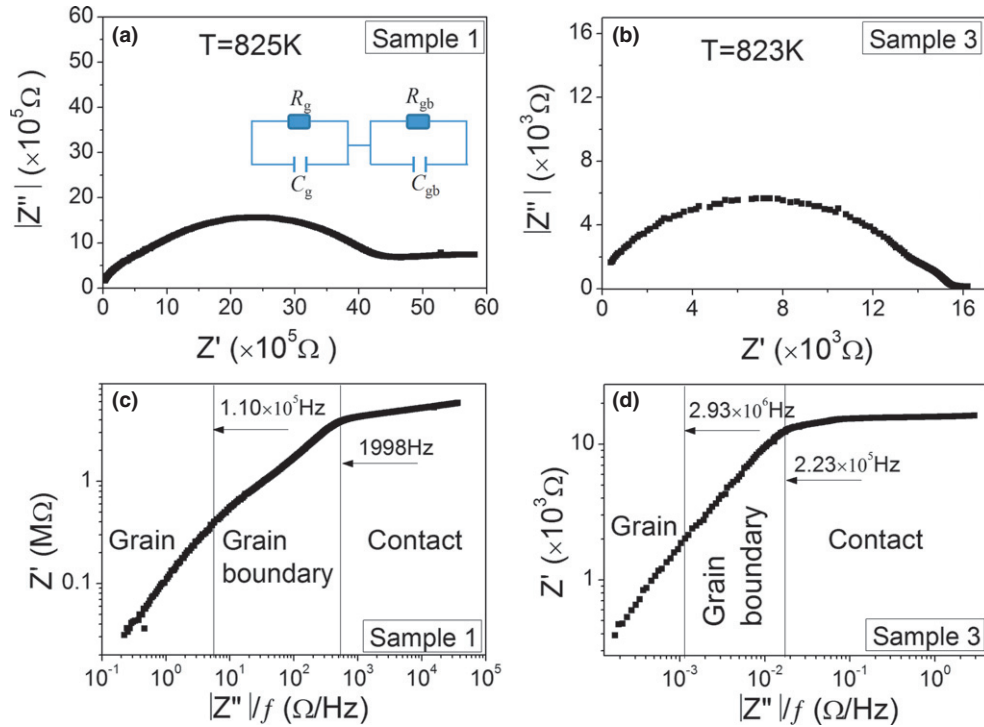


Fig. 9. (a) and (b) The Nyquist plots for samples 1 and 3, respectively. The data in (a) and (b) were replotted in (c) and (d), respectively, using the representation of Z' versus $-Z''/f$. The inset in Fig. 9(a) is the equivalent circuits.

Wagner relaxation. Heavy doping (20 at.%) can stabilize the cubic HfO_2 phase to room temperature, improve the conductivity, and reduce the grain-boundary capacitance. The grain response takes over the grain-boundary response and becomes the predominant contributor to the dielectric properties of the heavily doped sample.

Acknowledgments

The authors thank financial support from National Natural Science Foundation of China (Grant No 11404002 and 11404003) and Co-operative Innovation Research Center for Weak Signal-Detecting Materials and Devices Integration of Anhui University (Grant No Y01008411). This work was supported in part by the China Postdoctoral Science Foundation and Anhui Province Postdoctoral Science Foundation (Grant No. 2014M561805 and No.2014B007).

References

- D. Ceresoli and D. Vanderbilt, "Structural and Dielectric Properties of Amorphous ZrO_2 and HfO_2 ," *Phys. Rev. B.*, **74** [12] 125108, 6pp (2006).
- E. Cockayne, "Influence of Oxygen Vacancies on the Dielectric Properties of Hafnia: First-Principles Calculation," *Phys. Rev. B.*, **75** [9] 094103, 8pp (2007).
- G. Dutta, "A First-Principles Study of Enhanced Dielectric Responses in Ti and Ce Doped HfO_2 ," *Appl. Phys. Lett.*, **94** [1] 012907, 3pp (2009).
- K. Xiong, Y. Du, K. Tse, and J. Robertson, "Defect States in the High-Dielectric-Constant Gate Oxide HfSiO_4 ," *J. Appl. Phys.*, **101** [2] 244101, 7pp (2007).
- Y. Wang, F. Zahid, J. Wang, and H. Guo, "Structure and Dielectric Properties of Amorphous High- κ Oxides: HfO_2 , ZrO_2 , and Their Alloys," *Phys. Rev. B.*, **85** [22] 224110, 5pp (2012).
- N. Umezawa, et al., "Unique Behavior of F-Centers in High- κ Hf-Based Oxides," *Phys. B.*, **376-377** 392-4 (2006).
- A. M. Stoneham, et al., "Trapping, Self-Trapping and the Polaron Family," *J. Phys. Condens. Matter*, **19** [25] 255208, 22pp (2007).
- H. Takeuchi, D. Ha, and T.-J. King, "Observation of Bulk HfO_2 Defects by Spectroscopic Ellipsometry," *J. Vac. Sci. Technol., A*, **22** [4] 1337-41 (2004).
- N. N. Iosad, et al., "Dielectric Response of Sputtered Transition Metal Oxides," *J. Appl. Phys.*, **95** [12] 8087-91 (2004).
- B. Lee, T. Moon, T. G. Kim, D. K. Choi, and B. Park, "Dielectric Relaxation of Atomic-Layer-Deposited HfO_2 Thin Films From 1 kHz to 5 GHz," *Appl. Phys. Lett.*, **87** [1] 012901, 3pp (2005).
- H. S. Baik, et al., "Interface Structure and Non-Stoichiometry in HfO_2 Dielectrics," *Appl. Phys. Lett.*, **85** [4] 672-4 (2004).
- C. Mannequin, P. Gonon, C. Vallée, A. Bsiesy, H. Grampeix, and V. Jousseume, "Dielectric Relaxation in Hafnium Oxide: A Study of Transient

Currents and Admittance Spectroscopy in HfO_2 Metal-Insulator-Metal Devices," *J. Appl. Phys.*, **110** [10] 104108, 9pp (2011).

¹³O. Khaldi, F. Jomni, P. Gonon, C. Mannequin, and B. Yangui, "Investigation of Electrical Properties of HfO_2 Metal-Insulator-Metal (MIM) Devices," *Appl. Phys. A*, **116** [4] 1647-53 (2014).

¹⁴I. S. Han, et al., "A Study of Dielectric Relaxation and Capacitance Matching of $\text{Al}_2\text{O}_3/\text{HfO}_2/\text{Al}_2\text{O}_3$ MIM Capacitors," *IEEE Electron Device Lett.*, **34** [10] 1223-5 (2013).

¹⁵W. Luo, T. Yuan, Y. Kuo, J. Lu, and J. Yan, "Charge Trapping and Dielectric Relaxation in Connection With Breakdown of High- κ Gate Dielectric Stacks," *Appl. Phys. Lett.*, **88** [20] 202904, 3pp (2006).

¹⁶S. Mueller, C. Adelman, A. Singh, S. V. Elshocht, U. Schroeder, and T. Mikolajick, "Ferroelectricity in Gd-Doped HfO_2 Thin Films," *ECS J. Solid State Sci. Technol.*, **1** [6] N123-6 (2012).

¹⁷S. Mueller, et al., "Incipient Ferroelectricity in Al-Doped HfO_2 Thin Films," *Adv. Funct. Mater.*, **22** [11] 2414-7 (2012).

¹⁸J. Müller, et al., "Ferroelectricity in Yttrium-Doped Hafnium Oxide," *J. Appl. Phys.*, **110** [11] 114113, 5pp (2011).

¹⁹T. S. Böske, et al., "Phase Transitions in Ferroelectric Silicon Doped Hafnium Oxide," *Appl. Phys. Lett.*, **99** [11] 112904, 3pp (2011).

²⁰T. S. Böske, J. Müller, D. Bräuhäus, U. Schröder, and U. Böttger, "Ferroelectricity in Hafnium Oxide Thin Films," *Appl. Phys. Lett.*, **99** [10] 112903, 3pp (2011).

²¹X. Sang, E. D. Grimley, T. Schenk, U. Schroeder, and J. M. LeBeau, "On the Structural Origin of Ferroelectricity in HfO_2 Thin Films," *Appl. Phys. Lett.*, **106** [16] 162905, 4pp (2015).

²²C. K. Roy, M. Noor-A-Alam, A. R. Choudhuri, and C. V. Ramana, "Synthesis and Microstructure of Gd_2O_3 -doped HfO_2 Ceramics," *Ceram. Int.*, **38** [3] 1801-6 (2012).

²³T. Chen, S. Tekeli, R. P. Dillon, and M. L. Mecartney, "Phase Stability, Microstructural Evolution and Room Temperature Mechanical Properties of TiO_2 Doped 8 mol% Y_2O_3 Stabilized ZrO_2 (8Y-CSZ)," *Ceram. Int.*, **34** [2] 365-70 (2008).

²⁴M. A. Subramanian, L. Dong, N. Duan, B. A. Reisner, and A. W. Sleight, "High Dielectric Constant in $\text{ACu}_3\text{Ti}_4\text{O}_{12}$ and $\text{ACu}_3\text{Ti}_3\text{FeO}_{12}$ Phases," *J. Solid State Chem.*, **151** [2] 323-5 (2000).

²⁵K. J. Choi, et al., "Enhancement of Ferroelectricity in Strained BaTiO_3 Thin Films," *Science*, **306** [5698] 1005-9 (2004).

²⁶J. H. Haeni, et al., "Room-Temperature Ferroelectricity in Strained SrTiO_3 ," *Nature*, **430** [7001] 758-61 (2004).

²⁷C. Ang, Z. Yu, and L. E. Cross, "Oxygen-Vacancy-Related low-Frequency Dielectric Relaxation and Electrical Conduction in Bi: SrTiO_3 ," *Phys. Rev. B.*, **62** [1] 228-36 (2000).

²⁸H. S. Shulman, D. Damjanovic, and N. Setter, "Niobium Doping and Dielectric Anomalies in Bismuth Titanate," *J. Am. Ceram. Soc.*, **83** [3] 528-32 (2000).

²⁹O. Bidault, P. Goux, M. Kchikech, M. Belkaoui, and M. Maglione, "Space-Charge Relaxation in Perovskites," *Phys. Rev. B.*, **49** [12] 7868-73 (1994).

³⁰C. C. Wang, et al., "Oxygen-Vacancy-Related Dielectric Relaxations in SrTiO_3 at High Temperatures," *J. Appl. Phys.*, **113** [9] 094103, 9pp (2013).

³¹C. C. Wang, et al., "Dielectric Relaxations in Rutile TiO₂," *J. Am. Ceram. Soc.*, **98** [1] 148–53 (2015).

³²A. K. Jonscher, *Dielectric Relaxation in Solids*. Chelsea-Dielectric Press, London, 1983.

³³C. C. Wang, M. N. Zhang, K. B. Xu, and G. J. Wang, "Origin of High-Temperature Relaxor-Like Behavior in CaCu₃Ti₄O₁₂," *J. Appl. Phys.*, **112** [2] 034109, 7pp (2012).

³⁴W. Li, K. Chen, Y. Y. Yao, J. S. Zhu, and Y. N. Wang, "Correlation Among Oxygen Vacancies in Bismuth Titanate Ferroelectric Ceramics," *Appl. Phys. Lett.*, **85** [20] 4717–9 (2004).

³⁵C. C. Wang, Y. M. Cui, and L. W. Zhang, "Dielectric Properties of TbMnO₃ Ceramics," *Appl. Phys. Lett.*, **90** [1] 012904, 3pp (2007).

³⁶A. S. Nowick and B. S. Berry, *An Elastic Relaxation in Crystalline Solids*. Academic Press, New York and London, 1972.

³⁷G. H. Cao, L. X. Feng, and C. Wang, "Grain-Boundary and Subgrain-boundary Effects on the Dielectric Properties of CaCu₃Ti₄O₁₂ Ceramics," *J. Phys. D: Appl. Phys.*, **40** [9] 2899–905 (2007).

³⁸C. C. Wang, C. Wang, R. Zeng, and S. X. Dou, "Intergrain Connectivity of MgB₂ Ceramics Studied by Impedance Analysis," *J. Appl. Phys.*, **108** [2] 023901, 6pp (2010).

³⁹D. C. Sinclair and A. R. West, "Impedance and Modulus Spectroscopy of Semiconducting BaTiO₃ Showing Positive Temperature Coefficient of Resistance," *J. Appl. Phys.*, **68** [8] 3850–6 (1989).

⁴⁰T. B. Adams, D. C. Sinclair, and A. R. West, "Giant Barrier Layer Capacitance Effects in CaCu₃Ti₄O₁₂ Ceramics," *Adv. Mater.*, **14** [18] 1321–3 (2002).

⁴¹G. Catalan, "Magnetocapacitance Without Magnetoelectric Coupling," *Appl. Phys. Lett.*, **88** [10] 102902, 3pp (2006). □